

# Multi-energy CT Based on a Prior Rank, Intensity and Sparsity Model (PRISM)

Hao Gao<sup>1</sup>, Hengyong Yu<sup>2,3,4</sup>, Stanley Osher<sup>1</sup> and Ge Wang<sup>2,3,4</sup>

<sup>1</sup>Department of Mathematics, University of California, Los Angeles, CA 90095, USA

<sup>2</sup>Department of Radiology, Division of Radiologic Sciences, Wake Forest University Health Sciences, Winston-Salem, NC 27157, USA

<sup>3</sup>Biomedical Imaging Division, VT-WFU School of Biomedical Engineering and Sciences, Wake Forest University Health Sciences, Winston-Salem, NC 27157, USA

<sup>4</sup>Biomedical Imaging Division, VT-WFU School of Biomedical Engineering and Sciences, Virginia Tech., Blacksburg, VA 24061, USA

E-mail: haog@math.ucla.edu, hengyong-yu@ieee.org, sjo@math.ucla.edu, and ge-wang@ieee.org

**Abstract.** We propose a compressive sensing (CS) approach for multi-energy computed tomography (CT), namely PRISM. To further compress the multi-energy image for allowing the reconstruction with fewer CT data and less radiation dose, PRISM models a multi-energy image as the superposition of a low-rank matrix and a sparse matrix (with row dimension in space and column dimension in energy), where the low-rank matrix corresponds to the stationary background over energy that has low matrix rank, and the sparse matrix represents the rest of distinct spectral features that is often sparse. Distinct from previous methods, PRISM utilizes the generalized rank, .e.g., the matrix rank of tight frame transform of a multi-energy image, which offers a way to characterize the multi-level and multi-filtered image coherence across the energy spectrum. Besides, the energy-dependent intensity information can be incorporated into the PRISM in terms of the spectral curves for base materials, with which the restoration of the multi-energy image becomes the reconstruction of the energy-independent material composition matrix. In a word, PRISM utilizes prior knowledge on the generalized rank and sparsity of a multi-energy image, and intensity/spectral characteristics of base materials. Furthermore, we develop an accurate and fast split Bregman method for PRISM, and demonstrate the superior performance of PRISM relative to several competing methods in simulations.

## 1. Introduction

Since Hounsfield's Nobel Prize winning breakthrough, x-ray computed tomography (CT) has been widely applied in clinical and preclinical applications and produces a huge amount of tomographic grey-scale images. Currently, over 100 million medical CT scans are performed in USA alone annually, and a huge number of micro-CT scans are done in research institutions and pharmaceutical companies worldwide. However, the images are often insufficient to distinguish diagnostically crucial shading differences due to poor tissue contrast, inherent quantum noise and involved radiation dosage. Physically, the x-ray spectrum contains much information, and CT images need not be only in grey-scale. Just as television technology is now in true-color, as a natural extension of dual energy CT [1], the future of CT will be multi-energy, generating much richer information. The multi-energy CT is also referred to as spectral, spectroscopic, energy-selective or energy-sensitive CT. To convey the power of multi-energy CT vividly, we can also call it "true-color CT" occasionally although x-rays cannot be directly perceived at either soft or hard energies.

The x-ray detection technology is the key to achieve multi-energy CT. Roughly speaking, x-ray detectors can be categorized into two groups: energy-integrating and energy-discriminating. Almost exclusively, all current x-ray scanners use energy-integrating detectors where the interactions between

an x-ray beam and materials are accumulated over an entire energy spectrum. In typical energy-discriminating detectors [2-4], each photon above some minimum energy is counted, regardless of its energy. This capability can be utilized in a sophisticated way for energy discrimination. A primary example is the Medipix detector family. Particularly, a Medipix3 detector recognizes each x-ray photon along with its energy range effectively and efficiently [2]. Clearly, such multi-energy detectors give full spectral information, support novel contrast-enhanced studies [5, 6], and open new possibilities for functional, cellular and molecular imaging [7-10]. It is recognized that data collected in different spectral channels are not totally independent. For example, in the high energy region of the x-ray spectrum Compton scattering is dominant, and the attenuation coefficient is mainly proportional to the density of material. However, given the complexity of biological tissues this dependence does not mean the complete redundancy (e.g., due to Doppler broadening or electron binding energy and momentum). More importantly, the use of contrast agents of various K-edges (Figure 2) makes multi-energy CT definitely necessary, and clearly superior to dual-energy CT [6].

Parallel to the development of energy-discriminating detectors, an emerging theory – compressive sensing (CS) – was recently developed to capture compressible signals at a sampling rate much below the Nyquist rate and allow accurate reconstruction of these signals from sparse samples [11, 12]. Typically, CS starts by taking a limited number of samples, using a least correlated measurement matrix, and then the signal is exactly recovered with an overwhelming probability from the limited data via the  $L_1$  norm minimization [11, 12]. The major motivation for CS is that most signals are sparse under an appropriate basis. That is, a majority of their expansion coefficients with respect to the basis are equal to or close to zero. Through CS, it is sufficient to precisely reconstruct the image using undersampled data with roughly the same cardinality as the image sparsity. Consequently, sparser image representation allows accurate reconstruction with fewer data. Besides  $L_1$  sparsity (L1) [13], other popular choices for sparsity representation include total variation (TV) [14], combination of L1 and TV (L1+TV) [15, 16], wavelet [17, 18] and tight frame or framelet (TF) [19, 20]. As a generalization of L1+TV and wavelet, TF usually offers a sparser representation due to its redundant basis and multi-resolution structure [19, 20]. We will use TF for sparser representation.

In this article, we propose a compressive sensing (CS) approach for multi-energy CT, namely PRISM. To further compress the multi-energy image for allowing the reconstruction with fewer CT data and less radiation dose, PRISM models a multi-energy image as the superposition of a low-rank matrix and a sparse matrix (with row dimension in space and column dimension in energy), where the low-rank matrix corresponds to the stationary background over energy that has low matrix rank, and the sparse matrix represents the rest of distinct spectral features that is often sparse. Distinct from previous methods, PRISM utilizes the generalized rank, e.g., the matrix rank of tight frame transform of a multi-energy image, which offers a way to characterize the multi-level and multi-filtered image coherence across the energy spectrum. Besides, the energy-dependent intensity information can be incorporated into the PRISM in terms of the spectral curves for base materials, with which the restoration of the multi-energy image becomes the reconstruction of the energy-independent material composition matrix. (Depending on specific applications, the optimal selection of energies or spectral channels must be done to avoid matrix singularities and maximize image quality. However, in this feasibility study sufficiently many energy bins have been arbitrarily selected to keep all the intrinsic information.) In a word, PRISM utilizes prior knowledge on the generalized rank and sparsity of a multi-energy image, and intensity/spectral characteristics of base materials. Furthermore, we develop an accurate and fast split Bregman method for PRISM, and demonstrate the superior performance of PRISM relative to several competing methods in simulations.

The PRISM is motivated by the recent work on rank-sparsity incoherence [21], robust principle component analysis (RPCA) [22] and RPCA-4DCT model [23]. In rank-sparsity decomposition [21] and RPCA [22], the data matrix is decomposed into a low-rank part and a sparse part, and both parts can be recovered by minimizing the sum of the nuclear norm of the low-rank component and the  $L_1$  norm of the sparse component (subject to certain incoherence conditions). Similar models have been considered in various applications [24-31]. In the RPCA-4DCT model [23], a 4D spatiotemporal

object is modeled as a summation of a low rank matrix and a sparse matrix with the generalized sparsity in TF. Another difference of the RPCA-4DCT model is that the CT data are Radon transform or x-ray transform of an image through some ill-posed system matrix rather than directly from the image. In this article, the PRISM generalizes the previous methods, and is pertinent to multi-energy CT for using spectral priors. A distinct feature of the PRISM is that the image rank at consideration is generalized from the matrix rank of the multi-energy image to the matrix rank of the TF transform of the multi-energy image for characterizing multi-level and multi-filtered image coherence.

## 2. Methodology

### 2.1. Multi-energy CT

Consider a multi-energy image  $X$  with  $N_E$  spectral channels, i.e., a spectral sequence of spatial images,

$$X = \{X_i, i \leq N_E\}. \quad (2.1)$$

In 2D case with  $N_x$  pixels along x-axis and  $N_y$  pixels along y-axis,

$$X_i = \{x_{i,jk}, j \leq N_x, k \leq N_y\} \text{ or } X_i = \{x_{i,j}, j \leq N_S\}, \quad (2.2)$$

where the second  $j$  is a double index for convenience and  $N_S = N_x \cdot N_y$ .

In order to compute the image rank of  $X$ , we form  $X$  as a spatial spectral matrix with row dimension in space indexed by  $j$  and column dimension in energy indexed by  $i$ .

Let  $A$  be the system matrix [32] corresponding to the CT scanning geometry at consideration. Assuming additive Gaussian noise  $N$ , without downsampling, the acquired multi-energy data are

$$Y = \{Y_i = AX_i + N_i, i \leq N_E\}. \quad (2.3)$$

The objective of multi-energy CT is to recover  $X$  from  $Y$ . From a practical point of view in terms of radiation dose, the imaging by acquiring the least amount of CT data is favorable. That is we consider the undersampled problem

$$Y = \{Y_i = P_i(AX_i) + N_i, i \leq N_E\}, \quad (2.4)$$

where  $P_i$  denotes the undersampling pattern at the  $i$ th energy bin. In this study, we adopt the dynamic undersampling strategy [23]. To simplify the notation, we abbreviate (2.3) or (2.4) as

$$Y = AX + N. \quad (2.5)$$

### 2.2. Prior Work Related to PRISM

The original problems similar to the PRISM were considered for rank-sparsity incoherence [21] and RPCA [22]. The problem to recover principle component  $X_L$  (modeled as a low-rank matrix) from data  $Y$  with outliers  $X_S$  (modeled as a sparse matrix) is converted to the following minimization problem

$$(X_L, X_S) = \arg \min_{(X_L, X_S)} r \|X_L\|_* + \|X_S\|_1 \quad (2.6)$$

$$\text{Subject to } X_L + X_S = Y$$

When certain incoherence conditions are satisfied, both  $X_L$  and  $X_S$  can be uniquely recovered. Here the value of  $r$  (for the matrix with  $n_1$  rows and  $n_2$  columns) [22] is suggested to be

$$r = \sqrt{\max(n_1, n_2)}. \quad (2.7)$$

Inspired by the above idea, the RPCA-4DCT model was proposed for 4D CT [23]

$$(X_L, X_S) = \arg \min_{(X_L, X_S)} \|A(X_L + X_S) - Y\|^2 + \lambda_* \|X_L\|_* + \lambda_1 \|T_S(X_S)\|_1, \quad (2.8)$$

where  $T_S$  was chosen to be the TF transform [19, 20].

Two major differences between the RPCA-4DCT (2.8) and (2.6) are: (1) the data  $Y$  for RPCA-4DCT is the Radon transform or x-ray transform of  $X$  rather than a subset of  $X$ , and consequently the reconstruction of  $X$  is more challenging; (2) the sparsity of  $X_S$  is generalized in RPCA-4DCT under the proper sparsifying transform, such as TF.

### 2.3. PRISM: Rank-and-Sparsity Decomposition

Inspired by CS theory that sparser image representation allows the reconstruction with fewer data, we will choose the TF as the sparsifying basis since it is a generalization of several popular sparsity transforms, such as L1+TV and wavelet [19, 20].

On the other hand, the structural similarity shared by images within different energy bins can be utilized to further compress their representation. This spectral coherence can be mathematically characterized by the matrix rank of  $X$  over the spectral dimension. The lower the rank is, the more coherent the images are. Theories suggest that the data amount required for exact recovery of the images only needs to match their rank [33, 34].

However, the representation can be further sparsified by considering the rank-and-sparsity decomposition [21-23]! Therefore, the further reduction of CT data that are proportionally correlated to the radiation dose can be expected for multi-energy CT. In Figure 1 for example, despite the matrix being full rank and nonzero everywhere, it can be decomposed into a low-rank component and a sparse component. This simple observation (Figure 1) suggests an alternative view of the multi-energy image:  $X$  can be abstracted as the superposition of the background component, which is spectrally coherent, and the variation component, which is spatially sparse. Now, we generalize previous models into a coherence-and-variation decomposition model, namely PRISM, aiming for sparser representation of the multi-energy image to allow a higher undersampling factor or better image quality with the same data.

That is we model  $X$  as the sum of two matrices  $X_L$  and  $X_S$ , i.e.,

$$X = X_L + X_S, \quad (2.9)$$

and enforce the following regularization

$$R(X_L, X_S) = \lambda_* \|T_L(X_L)\|_* + \lambda_1 \|T_S(X_S)\|_1 + \lambda_r \|X\| \quad (2.10)$$

in PRISM

$$(X_L, X_S) = \underset{(X_L, X_S)}{\operatorname{argmin}} \|A(X_L + X_S) - Y\|^2 + R(X_L, X_S). \quad (2.11)$$

In (2.10),  $\|\cdot\|_*$  is the nuclear norm for the rank regularization on  $X_L$  with the parameter  $\lambda_*$ . Let  $\{\sigma_i\}$  be the singular values of  $X$ , then

$$\|X\|_* = \sum_i \sigma_i. \quad (2.12)$$

$\|\cdot\|_1$  is the L<sub>1</sub> norm for the sparsity regularization on  $X_S$  with the parameter  $\lambda_1$ . Let  $\{x_i\}$  be the entries of  $X$ , then

$$\|X\|_1 = \sum_i |x_i|. \quad (2.13)$$

$\|\cdot\|$  is a regularizing norm on the total image  $X$  to preserve its smoothness and contrast, with the parameter  $\lambda_r$ . Since we regularize the image rank of  $X_L$  and the image sparsity of  $X_S$ , we name  $X_L$  the low-rank component and  $X_S$  the sparse component. In multi-energy CT,  $X_L$  often corresponds to stationary background or slow variation while  $X_S$  characterizes spectral jumps, such as K-edges.

More importantly, we consider the generalized rank and sparsity in PRISM:  $T_L$  (resp.  $T_S$ ) represents a transform for the strengthened rank regularization (resp. sparsity regularization). In particular, we consider the rank of the TF transform of  $X_L$  and the sparsity of  $X_S$  under TF.

### 2.4. PRISM: Sparsity

In this study, we choose the piecewise-constant B-spline TF transform  $W$  that can be constructed from two refinement masks: the averaging mask and the differencing mask. Consequently, the 2D refinement masks constructed from the tensor product are

$$w_{0,0} = \frac{1}{4} \begin{bmatrix} 1 & 1 \\ 1 & 1 \end{bmatrix}, w_{0,1} = \frac{1}{4} \begin{bmatrix} 1 & -1 \\ 1 & -1 \end{bmatrix}, w_{1,0} = \frac{1}{4} \begin{bmatrix} 1 & 1 \\ -1 & -1 \end{bmatrix}, \text{ and } w_{1,1} = \frac{1}{4} \begin{bmatrix} 1 & -1 \\ -1 & 1 \end{bmatrix}. \quad (2.14)$$

Let  $x$  be a 2D image with the standard 2D indices, i.e.,  $x = \{x_{jk}, j \leq N_x, k \leq N_y\}$ . The multilevel TF transform of  $x$  up to  $L$  levels is

$$Wx = \left[ \underbrace{[Wx]_{0,1}^1 \ [Wx]_{1,0}^1 \ [Wx]_{1,1}^1 \cdots}_{\text{Level 1}} \underbrace{[Wx]_{0,1}^l \ [Wx]_{1,0}^l \ [Wx]_{1,1}^l \cdots}_{\text{Level } l} \cdots \underbrace{[Wx]_{0,1}^L \ [Wx]_{1,0}^L \ [Wx]_{1,1}^L}_{\text{Level } L} x^L \right], \quad (2.15)$$

with  $x^0 = x$  and the following convolutions

$$x^l = w_{0,0}^l * x^{l-1}, [Wx]_{0,1}^l = w_{0,1}^l * x^l, [Wx]_{1,0}^l = w_{1,0}^l * x^l, [Wx]_{1,1}^l = w_{1,1}^l * x^l, 1 \leq l \leq L. \quad (2.16)$$

Here the dependence of the mask on the level comes from the choice of TF without downsampling  $x^l$ . That is, instead of downsampling  $x^l$ , we dilute the masks (2.14) so that

$$w_{i_1, i_2}^l = D^l w_{i_1, i_2}, 0 \leq i_1, i_2 \leq 1, \quad (2.17)$$

where  $D^l w$ 's are  $(2^l + 1) \times (2^l + 1)$  matrices with four nonzero entries defined by

$$D^l w = \begin{bmatrix} w(1,1) & \cdots & w(1,2) \\ \cdots & \cdots & \cdots \\ w(2,1) & \cdots & w(2,2) \end{bmatrix} \text{ for } w = \begin{bmatrix} w(1,1) & w(1,2) \\ w(2,1) & w(2,2) \end{bmatrix}. \quad (2.18)$$

On the other hand the transpose of TF is defined by

$$W^T(Wx) = x^L + \sum_{l=1}^L ([Wx]_{0,1}^l + [Wx]_{1,0}^l + [Wx]_{1,1}^l). \quad (2.19)$$

One can show that TF has a left inverse [35], i.e.,

$$W^T(Wx) = x. \quad (2.20)$$

Now, let us define the TF norm of a single 2D image as

$$\|Wx\|_1 = \|x^L\|_1 + \sum_{l=1}^L \{ \| [Wx]_{1,0}^l \|_1 + \| [Wx]_{1,1}^l \|_1 \}, \quad (2.21)$$

with

$$[Wx]_{1,1}^l = \sqrt{([Wx]_{0,1}^l)^2 + ([Wx]_{1,0}^l)^2} \text{ and } [Wx]_{1,2}^l = [Wx]_{1,1}^l. \quad (2.22)$$

Here the second term of (2.21) is to make the regularization isotropic with respect to x-y coordinate that has the same spirit as the isotropic TV norm.

Please notice that TF (2.21) generalizes TV in the sense that its 2<sup>nd</sup> term corresponds to TV; it generalizes L1+TV since the first term corresponds to L1; it also generalizes the wavelet transform since TF often forms the redundant basis rather than the orthonormal basis. On the other hand, due to the property (2.20), the algorithm with TF regularization is in general faster than using the transform without left inverse, such as TV, since it would require additional computation of  $W^T W$  then. We will further clarify this advantage of TF in the solution algorithm.

Consequently, we define the TF norm of the multi-energy image  $X$  (2.1) by

$$\|WX\|_1 = \sum_{i=1}^{N_E} \|WX_i\|_1. \quad (2.23)$$

Here we select the regularization on both  $X_S$  and  $X$  in (2.10) to be the TF norm (2.23), i.e.,

$$\|T_L(X_S)\|_1 = \|WX_S\|_1 \text{ and } \|X\| = \|WX\|_1. \quad (2.24)$$

### 2.5. PRISM: Rank

Distinct from previous work, PRISM considers the rank regularization in the transform domain as well. In this study, we regularize the rank of the TF transform of  $X$ , i.e.,

$$\|T_L(X_L)\|_* = \|WX_L\|_*, \quad (2.25)$$

with the nuclear norm in the TF basis defined as

$$\|WX\|_* = \|X^L\|_* + \sum_{l=1}^L (\|[WX]_1^l\|_* + \|[WX]_2^l\|_*). \quad (2.26)$$

That is we compute the TF transform (2.15) of  $X_i$ 's from  $X_L$  and reorganize them into groups of matrices corresponding to different TF levels and masks, i.e.,

$$\begin{aligned} [WX]_1^l &= \left[ \sqrt{([WX]_{1,0,1}^l)^2 + ([WX]_{1,1,0}^l)^2} \quad \cdots \quad \sqrt{([WX]_{N_E,0,1}^l)^2 + ([WX]_{N_E,1,0}^l)^2} \right] \\ [WX]_2^l &= \left[ [WX]_{1,1,1}^l \quad \cdots \quad [WX]_{N_E,1,1}^l \right] \quad \text{and} \quad X^L = \left[ X_1^L \quad \cdots \quad X_{N_E}^L \right] \quad l \leq L \end{aligned} \quad (2.27)$$

This generalized rank allows more freedom in applications. For example, in multi-energy CT, the similarity across spectral channels is more in structures (boundaries, contours, and edges) rather than in images (gray-scale shading). On the other hand, the rank of the multi-energy image after the TF transform focuses on the structural features, while the rank of the image itself correlates energy-dependent gray shading variations. Clearly, it is more appropriate to regularize the rank of the structures through TF transform. Besides, TF transform offers a way to characterize the multi-level and multi-filtered image coherence through (2.26).

### 2.6. PRISM: Intensity/Spectral Priors

Spectral knowledge can be incorporated in the PRISM for better performance. Suppose that we know the intensity (linear attenuation coefficient) curves of base materials with respect to the energy,

$$B = \{b_{mi}, m \leq N_B, i \leq N_E\}, \quad (2.28)$$

where  $N_B$  is the number of base materials, and  $b_{mi}$  the attenuation coefficient of the  $m$ th material at the  $i$ th energy. Using the intensity/spectral priors  $B$ , we have an alternative representation of  $X$ . That is, the attenuation at the  $j$ th pixel for the  $i$ th energy is a linear combination of  $b_{mi}$ , i.e.,

$$x_{ji} = \sum_m z_{jm} b_{mi}, \quad (2.29)$$

or in the matrix form

$$X = ZB, \quad (2.30)$$

where  $Z$  is now a material composition matrix with its row dimension in a spatial variable and column dimension in a material variable, i.e.,

$$Z = \{z_{jm}, j \leq N_S, m \leq N_B\}. \quad (2.31)$$

With intensity/spectral priors, the reconstruction of  $X$  is a consequence of the reconstruction of  $Z$ . The most apparent benefit of (2.30) is that  $Z$  is independent of energy. Moreover, all  $z_{ik}$ 's are between 0 and 1 and therefore the image representation in  $Z$  is robust in terms of image contrast. On the contrary,  $X$  is spectrally dependent; the values of  $x_{ij}$ 's may differ greatly due to the spectral dependence.

Similarly, we have the rank-and-sparsity decomposition for  $Z$

$$Z = Z_L + Z_S. \quad (2.32)$$

Again,  $Z_L$  (resp.  $Z_S$ ) is the low-rank (resp. sparse) component with respect to the proper basis.

However, we still regularize  $Z$  in the image domain, i.e.,

$$R(Z_L, Z_S) = \lambda_* \|T_L(Z_L B)\|_* + \lambda_1 \|T_S(Z_S B)\|_1 + \lambda_t \|X\|. \quad (2.33)$$

With (2.33), we have transformed the original PRISM into an enhanced PRISM with the reconstruction of the spectrally independent variable  $Z$ .

More generally, if the base materials are partially known, we have a hybrid representation of  $X$  as follow,

$$X = (X_L + Z_L B) + (X_S + Z_S B), \quad (2.34)$$

Where  $B$  represents the partial intensity/spectral priors,  $X_L$  (resp.  $Z_L$ ) corresponds to the known materials (resp. the remaining portion) of the low-rank component, and  $X_S$  (resp.  $Z_S$ ) corresponds to the

known materials (resp. the remaining portion) of the sparse component. Consequently, the regularization with the partial priors is

$$R(X_L, Z_L, X_S, Z_S) = \lambda_* \|T_L(X_L + Z_L B)\|_* + \lambda_1 \|T_S(X_S + Z_S B)\|_1 + \lambda_t \|X\|, \quad (2.35)$$

where  $X$  is related to  $X_L, X_S, Z_L$  and  $Z_S$  through (2.34).

In summary, we have proposed three variants of the generic PRISM: (1) the PRISM without intensity/spectral priors defined by (2.10), (2) the PRISM with intensity/spectral priors of all the base materials as defined by (2.33), and (3) the PRISM with intensity/spectral priors for only part of the base materials as defined by (2.35). Other variants of the PRISM can be similarly defined. For example, when we have statistical knowledge of spatial and/or spectral characteristics of classes under investigation, which can be learned from a training dataset, we can define the corresponding PRISM-based inverse problems.

### 2.7. Methods for Comparison

To show the superiority of PRISM over several other methods for the multi-energy CT, we will first compare the following PRISM

$$(X_L, X_S) = \arg \min_{(X_L, X_S)} \frac{1}{2} \|AX - Y\|_2^2 + \lambda_* \|X_L\|_* + \lambda_1 \|WX_S\|_1 + \lambda_t \|WX\|_1, \quad (2.36)$$

with  $L_2$  regularization (L2)

$$X = \arg \min_X \|AX - Y\|_2^2 + \lambda \|X\|_2^2, \quad (2.37)$$

TF regularization (TF)

$$X = \arg \min_X \frac{1}{2} \|AX - Y\|_2^2 + \lambda \|WX\|_1, \quad (2.38)$$

rank regularization (LR)

$$X = \arg \min_X \frac{1}{2} \|AX - Y\|_2^2 + \lambda \|X\|_*, \quad (2.39)$$

and simultaneous TF and rank regularization (TFLR)

$$X = \arg \min_X \frac{1}{2} \|AX - Y\|_2^2 + \lambda_1 \|WX\|_1 + \lambda_* \|X\|_*. \quad (2.40)$$

Second, to show the superiority of PRISM with generalized rank, we will compare (2.36) with

$$(X_L, X_S) = \arg \min_{(X_L, X_S)} \frac{1}{2} \|AX - Y\|_2^2 + \lambda_* \|WX_L\|_* + \lambda_1 \|WX_S\|_1 + \lambda_t \|WX\|_1. \quad (2.41)$$

Last, we will compare PRISM without priors (2.36) with PRISM with partial spectral priors

$$(X_L, Z_L, X_S, Z_S) = \arg \min_{(X_L, Z_L, X_S, Z_S)} \frac{1}{2} \|AX - Y\|_2^2 + \lambda_* \|X_L + Z_L B\|_* + \lambda_1 \|W(X_S + Z_S B)\|_1 + \lambda_t \|WX\|_1, \quad (2.42)$$

and PRISM with full spectral priors

$$(Z_L, Z_S) = \arg \min_{(Z_L, Z_S)} \frac{1}{2} \|AX - Y\|_2^2 + \lambda_* \|Z_L B\|_* + \lambda_1 \|W(Z_S B)\|_1 + \lambda_t \|WX\|_1. \quad (2.43)$$

### 2.8. PRISM: Solution Algorithm by Split Bregman Method

Here we consider the solution algorithm for the following convex minimization problem

$$(X_L, X_S) = \arg \min_{(X_L, X_S)} \frac{1}{2} \|A(X_L + X_S) - Y\|_2^2 + \lambda_* \|WX_L\|_* + \lambda_1 \|WX_S\|_1, \quad (2.44)$$

based on Split Bregman method [36-38], which is simple-to-implement, yet particularly accurate and efficient for L1-type optimization problems [23, 39], such as (2.44). The solution algorithms for other variants of PRISM and other models can be developed in a similar fashion.

For improved accuracy, we minimize (2.44) with the regularization term replaced by its Bregman distance, and simplify it to the add-residual-back iterative scheme by introducing a dummy variable  $f$ . To efficiently handle non-differentiable TF norms, we first change TF norms into L1 norms by introducing the dummy variables  $d_L=WX_L$  and  $d_S=WX_S$ , and relax the constrained optimization into an unconstrained optimization. Then we use the similar add-residual-back iterative scheme to relax L1 norms into L2 norms by introducing the dummy variables  $v_L$  and  $v_S$ . That is, with zero initial guesses (i.e.,  $X_L^0=X_R^0=0, f^0=0$ , and  $d_L^0=v_L^0=d_S^0=v_S^0=0$ ), the solution algorithm for (2.44) consists of a single iteration loop with the following three steps

$$(X_L^{n+1}, X_S^{n+1}) = \arg \min_{(X_L, X_S)} \| A(X_L + X_S) - Y + f^n \|_2^2 + \mu_* \| WX_L - d_L^n + v_L^n \|_2^2 + \mu_1 \| WX_S - d_S^n + v_S^n \|_2^2, \quad (2.45)$$

$$f^{n+1} = f^n + A(X_L^{n+1} + X_S^{n+1}) - Y; \\ d_S^{n+1} = \arg \min_{d_S} \frac{1}{2} \| WX_S^{n+1} + v_S^n - d_S \|_2^2 + \frac{\lambda_1}{\mu_1} \| d_S \|_1, \quad (2.46)$$

$$v_S^{n+1} = v_S^n + WX_S^{n+1} - d_S^{n+1}; \\ d_L^{n+1} = \arg \min_{d_L} \frac{1}{2} \| WX_L^{n+1} + v_L^n - d_L \|_2^2 + \frac{\lambda_*}{\mu_*} \| d_L \|_*, \quad (2.47)$$

$$v_L^{n+1} = v_L^n + WX_L^{n+1} - d_L^{n+1}.$$

The convergence of this iterative scheme can be established by mimicking the proofs in [38].

The first step (2.45) is equivalent to an iteration step in a typical L<sub>2</sub> minimization problem, and its solution can be derived from the optimal condition, i.e.,

$$A^T A(X_L + X_S) + \mu_* X_L = A^T (Y - f^n) + \mu_* W^T (d_L^n - v_L^n) \\ A^T A(X_L + X_S) + \mu_1 X_S = A^T (Y - f^n) + \mu_1 W^T (d_S^n - v_S^n) \quad (2.48)$$

Please note that if it were not TF transform with  $W^T W=1$ , we may need to add  $W^T W$  in front of the second terms on the left-hand side of (2.48). Here we use the conjugate gradient (CG) method for solving the resultant linear system without explicitly formulating the linear system matrix, for which  $A^T A X$  often dominates the computational cost. Since the linear system is symmetric positive definite, CG gives the exact solution after a few iterations. Again, if it were not TF norm with  $W^T W=1$ , one may have to compute  $W^T W X$  during each CG inner iteration.

The second step (2.46) consists of the following scalar subproblems according to (2.21) for each  $i \leq N_E \times N_S$ ,

$$([d]_{0,1,i}^l, [d]_{1,0,i}^l) = \arg \min_{([d]_{0,1,i}^l, [d]_{1,0,i}^l)} \frac{1}{2} ([Y]_{0,1,i}^l - [d]_{0,1,i}^l)^2 + \frac{1}{2} ([Y]_{1,0,i}^l - [d]_{1,0,i}^l)^2 + \lambda^l |[d]_{1,1,i}^l|, l \leq L, \quad (2.49)$$

$$[d]_{1,1,i}^l = \arg \min_{[d]_{1,1,i}^l} \frac{1}{2} ([Y]_{1,1,i}^l - [d]_{1,1,i}^l)^2 + \lambda^l |[d]_{2,i}^l|, l \leq L, \quad (2.50)$$

$$d_i^L = \arg \min_{d_i^L} \frac{1}{2} (Y_i^L - d_i^L)^2 + \lambda^L |d_i^L|, \quad (2.51)$$

where the subscript ‘‘S’’ is neglected for clarity,  $\lambda = \lambda_l / \mu_l$ ,  $Y = WX_S^{n+1} + v_S^n$ , and the dependence of  $\lambda$  on the level is to balance the shrinkage at different levels, i.e.,  $\lambda^l = \lambda^0 / 2^l$ . And the solution of (2.49)-(2.51) can be solved by considering the following problem with the scalars  $x$  and  $y$



$$\{x_i, i \leq D\} = \arg \min_{(\{x_i, i \leq D\})} \frac{1}{2} \sum_{i=1}^D (x_i - y_i)^2 + \lambda \sqrt{\sum_{i=1}^D x_i^2}. \quad (2.52)$$

Its solution is given by the so-called generalized shrinkage formula [37],

$$x_i = S_\lambda(y_i) = \max(y^* - \lambda, 0) \frac{y_i}{y^*}, i \leq D, \quad (2.53)$$

with  $y^*$  defined as

$$y^* = \sqrt{\sum_{i=1}^D y_i^2}. \quad (2.54)$$

The third step (2.47) consists of the following matrix subproblems according to (2.25)

$$([d]_{0,1}^l, [d]_{1,0}^l) = \arg \min_{([d]_{0,1}^l, [d]_{1,0}^l)} \frac{1}{2} \|[Y]_{0,1}^l - [d]_{0,1}^l\|_2^2 + \frac{1}{2} \|[Y]_{1,0}^l - [d]_{1,0}^l\|_2^2 + \lambda_l \|[d]_1^l\|_*, l \leq L, \quad (2.55)$$

$$[d]_{1,1}^l = \arg \min_{[d]_{1,1}^l} \frac{1}{2} \|[Y]_{1,1}^l - [d]_{1,1}^l\|_2^2 + \lambda_l \|[d]_2^l\|_*, l \leq L, \quad (2.56)$$

$$d^L = \arg \min_{d^L} \frac{1}{2} \|Y^L - d^L\|_2^2 + \lambda_L \|d^L\|_*, \quad (2.57)$$

where the subscript “ $L$ ” is neglected for clarity,  $\lambda = \lambda_*/\mu_*$  and  $Y = WX_L^{n+1} + v_L^n$ . And the solution of (2.55)-(2.57) can be solved by considering the following problem with the matrices  $x$  and  $y$

$$\{x_i, i \leq D\} = \arg \min_{(\{x_i, i \leq D\})} \frac{1}{2} \sum_{i=1}^D \|x_i - y_i\|_2^2 + \lambda \sqrt{\sum_{i=1}^D x_i^2} \|. \quad (2.58)$$

The proof in the Appendix shows that the solution of (2.58) is given by the following generalized singular value thresholding (G-SVT) formula,

$$x_i = T_\lambda(y_i) = [U \cdot \text{diag}(\max(\sigma - \lambda, 0)) \cdot V^T] \frac{y_i}{y}, i \leq D, \quad (2.59)$$

with  $y^*$  from the following point-wise operation, and  $U, V, \sigma$  as its orthonormal vectors and singular values,

$$y^* = \sqrt{\sum_{i=1}^D y_i^2} \text{ and } y^* = U \cdot \text{diag}(\sigma) \cdot V^T. \quad (2.60)$$

In (2.60), the operation with respect to  $y_i$  (resp.  $y^*$ ) is the point-wise multiplication (resp. division), and the convention is that  $y_i/y^*$  is zero whenever  $y^*$  is zero. Here the G-SVT step is computationally negligible comparing with (2.48) since the number of the spectral dimension is usually only a few, which is much less than that of the spatial dimension.

Now we summarize the solution algorithm as follow

$$\begin{aligned} (X_L^{n+1}, X_S^{n+1}) &= CG(A, Y, f^n, d^n, v^n), \\ f^{n+1} &= f^n + AX^{n+1} - Y; \\ d_S^{n+1} &= S_{\lambda_1/\mu_1}(WX_S^{n+1} + v_S^n), \\ v_S^{n+1} &= v_S^n + WX_S^{n+1} - d_S^{n+1}; \\ d_L &= T_{\lambda_*/\mu_*}(WX_L^{n+1} + v_L^n), \\ v_L^{n+1} &= v_L^n + WX_L^{n+1} - d_L^{n+1}. \end{aligned} \quad (2.61)$$

where CG represents the solution to the  $L_2$  subproblem (2.45), the generalized shrinkage formula  $S$  is given by (2.53), and the G-SVT solution  $T$  is given by (2.59). Please note that the step by G-SVT (2.59)

is computationally negligible since the number of columns of the matrix considered here is only a few. The dominant step is the first one for solving the  $L_2$  subproblem. Due to its iterative nature, empirically it is not necessary to solve each CG step with very high accuracy in order for the whole loop to achieve fast convergence. In our study, CG with 10 inner iterations is adequate for (2.61) to reach an acceptable reconstruction accuracy within 30 outer iterations.

Regarding the regularization parameters, the following formulas are recommended

$$r = \sqrt{\max(n_1, n_2)}, \lambda_* = r\lambda_1, \mu_* = \mu_1 = \lambda_1, \quad (2.62)$$

where  $n_1$  ( $n_2$ ) are the number of rows (columns) of the image matrix  $X$ , and the choice of  $r$  is suggested by [22]. Moreover, the proper scaling is recommended for energy-dependent regularization since the scale of  $X$  may vary substantially across different energies. That is, we weight  $r$  by the  $L_2$  norm of the measurement  $Y$  at different energies, i.e.,

$$r_i = r \frac{\|Y_i\|_2}{\max_i \|Y_i\|_2}, i \leq N_E, \quad (2.63)$$

where  $r_i$  is the regularizing parameters for the  $i$ th energy bin. Therefore, the only parameters to be determined are  $\lambda_j$ . Empirically, it was found that  $\lambda_j \in [0.1, 1]$  provides the satisfactory performance in terms of both accuracy and speed.

### 3. Results

In this proof-of-concept study, for simplicity we simulated in 2D, rather than 3D, on a 256 by 256 spatial grid. Projection data were acquired in the equidistant fan beam scanning geometry with a scanning trajectory of a 10cm radius, being similar to a typical micro-CT setting. Only 16 views of data per energy bin were simulated using dynamic undersampling strategy [23]. And then the data were contaminated with 1% Gaussian noise. Here,  $L=2$  in the TF regularization.

We first compared the PRISM (2.36) with L2 (2.37), TF (2.38), LR (2.39), and TFLR (2.40). We also compared with the PRISM (2.36) with  $\lambda_i=0$  to show the difference due to the regularization on the entire image. See Figure 3 and 4 for the results. Here we did not compare with the direct reconstruction by the filtered backprojection (FBP), which generally gives worse accuracy than L2 when reconstructing with undersampled data. Then we evaluated the effect of generalized rank in PRISM by comparing (2.36) and (2.41). See Figure 5 and 6 for the results. Finally we evaluated the effect of specific intensity/spectral priors by comparing (2.36), (2.42) and (2.43). See Figure 7 and 8 for the results.

Except L2, which is differentiable and therefore can be solved with iterations with a single step that is similar to (2.45), all the other aforementioned models can be solved through split Bregman iterations similar to (2.61). Since the major computational cost with all the models is from the  $L_2$  subproblem (2.45), the total computational time is approximately proportional to the number of iterations. It was found that roughly 30 iterations together with the parameters specified by (2.62) and (2.63) were sufficient, with each reconstruction that took 1 to 2 minutes on the MATLAB platform on a desktop with Intel CPU E6850 3.0GHz. In other words, all the models except L2 were similar in terms of computational cost, but L2 failed to provide the satisfactory image quality regardless of the number of iterations.

#### 3.1. Phantom

A circular phantom of a 2.0cm diameter (Figure 2(a)) was designed to simulate a mouse, and it contained 14 circular inclusions each of which was made of a different material (Table 1). While Objects 1-8 were used to simulate the unique biologically relevant spectral characteristics, Objects 9-14 were intended to quantify the image resolution.

The NIST Report 5632 by Hubbell and Seltzer provided tables of x-ray mass attenuation coefficients and mass energy-absorption coefficients from 1 keV to 20 MeV for Elements  $Z = 1$  to 92

and 48 additional substances of dosimetric interest (<http://www.nist.gov/pml/data/xraycoef/index.cfm>). Based on these tables, Tuszynski published an open source package (<http://www.mathworks.com/matlabcentral/fileexchange/12092-photonattenuation-2>) to interpolate the attenuation and energy absorption coefficients for x-rays and gamma-rays in various materials including mixtures and compounds, with additional functions that provided x-ray attenuation and absorption mean free paths and x-ray fractional transmission and absorption coefficients in these 140 materials, homogenous mixtures and chemical compounds based on these materials. The attenuation coefficients used in this study were interpolated using Tuszynski's open source package. The spectral curves of the attenuation coefficients of 8 typical materials are plotted in Figure 2(b). In particular, in this proof-of-concept study, we assumed there were 12 energy channels centering at 24Kev, 30Kev, 36Kev, 42Kev, 48Kev, 54Kev, 60Kev, 66Kev, 72Kev, 78Kev, 84Kev and 90Kev respectively. And we also assumed that each channel was strictly selective around its central energy. Therefore, it was not necessary to specify the x-ray spectrum. Figure 3-8 shows the attenuation maps at the 1<sup>st</sup>, 4<sup>th</sup>, 8<sup>th</sup> and 12<sup>th</sup> energy bins, where the images in each row have the same display window as the first phantom image in that row.

### 3.2. PRISM v.s. other methods

The reconstruction results with various methods are shown in Figure 3 with regional zoom-in details in Figure 4. As shown in these two figures, the result from L2 was blurred and full of artifacts; TF improved the image quality significantly for this piecewise-constant phantom by reducing its blurring and artifacts, however failed to resolve Object 13 and blurred Object 12; despite the alleviated blurring, strong artifacts still presented for LR that prevented it from visualizing Object 12 and 13; the improvement from TFLR was between TF and LR; PRISM with  $\lambda_i=0$  resolved Object 13, but still with some artifacts that are particularly notable in Figure 4; finally, PRISM with the total image regularization offered the best image quality with much reduced artifacts, the best contrast for Object 12 and clearly resolved Object 13.

### 3.3. PRISM with generalized rank

The comparison of PRISM with generalized rank and PRISM with image rank is shown in Figure 5 with regional zoom-in details in Figure 6. As shown in these two figures, the use of the rank of TF transform of the multi-energy image (2.26) indeed improved the image quality with much fewer artifacts, better contrast for Object 13 and better resolution for Object 14. Besides, the use of generalized rank offered a better decomposition into the low-rank component and the sparse component.

### 3.4. PRISM with intensity/spectral priors

The comparison of PRISM with no, partial, and full priors is shown in Figure 7 with regional zoom-in details in Figure 8. For clarity, the image rank was used instead of the generalized rank. Here the full intensity/spectral prior matrix  $B$  defined by (2.28) was directly obtained from the spectral curves in Figure 2(b), and the partial prior matrix consisted of 5 known mixed materials as listed in Table 1 (i.e., Object 4-14). As shown in these two figures, the use of the priors clearly improved image quality, such as the clearly resolved Object 14; with full spectral priors, PRISM reconstructed almost the same image as the phantom.

## 4. Discussions and Conclusion

A natural extension of the PRISM for multi-energy CT and 4D CT is the development for 5D CT, i.e., spatial, temporal and spectral CT. A similar matrix decomposition model can be established, for example, with the row dimension in a spatial variable (3D) and the column dimension in a temporal spectral variable (2D). That is, the stationary background over time and across energy can be extracted as the low-rank component, while the distinct spectral features and temporal changes can be captured

as the sparse component. Again, both components can be with respect to the proper transform, and additional spectral and temporal priors can be utilized as well.

Most interestingly, we can and should view a 5D object as a spatial, temporal and spectral tensor, which should be more appropriate for 5D CT (and for 4D CT and multi-energy CT as well). However, this may require advanced tensor based mathematical tools and next-generation algorithms that could be fundamentally different from that for matrix algebra. This is an exciting direction for applied mathematical research.

Moreover, PRISM and the aforementioned ideas can be translated for interior tomography [40-43], a theoretically justified methodology with which an interior region of interest (ROI) can be theoretically exactly reconstructed only from local projection data directly associated with paths through this ROI. While solving such an interior problem would conventionally require the whole body x-ray illumination, by its nature interior tomography promises to reduce radiation dose, handle large objects, and accelerate imaging speed. The robustness of interior tomography is an active research area. Newer types of algorithms are needed, and can be developed based on the work reported here. For example, similar models and algorithms can be carried over for interior multi-energy CT or interior 5D CT.

In conclusion, we have proposed a novel rank-and-sparsity decomposition model – PRISM – for multi-energy CT. The PRISM approach synergistically utilizes prior knowledge on the sparsity and rank of the multi-energy image up to the proper transform, and energy-dependent intensity characteristics of structures and/or base materials. Also, we have developed an accurate and fast solution algorithm based on split Bregman method, and numerically demonstrated the merits of our approach. Further work is under way, including algorithmic optimization and experimental validation.

### **Acknowledgments**

This work was partially supported by the NSF/MRI program CMMI-0923297, NIH/NIBIB grant EB011785, and NIH/NIBIB grant EB013387. The authors thank Drs. Phil Butler and Anthony Butler for valuable discussions and inputs on the multi-energy micro-CT.

## Appendix: Solution of (2.58)

**Theorem.** The solution of the following minimization problem

$$\{X_i, i \leq D\} = \underset{\{(X_i, i \leq D)\}}{\operatorname{argmin}} \frac{1}{2} \sum_{i=1}^D \|X_i - Y_i\|_2^2 + \lambda \left\| \sqrt{\sum_{i=1}^D X_i^2} \right\|_*, \lambda > 0 \quad (\text{A.1})$$

is uniquely determined by the generalized singular value thresholding (G-SVT) formula, i.e.,

$$X_i = T_\lambda(Y_i) = [U \cdot \operatorname{diag}(\max(\sigma - \lambda, 0)) \cdot V^T] \frac{Y_i}{Y^*}, i \leq D, \quad (\text{A.2})$$

with  $Y^*$  defined by the following point-wise operation, and  $U, V, \sigma$  as its orthonormal vectors and singular values respectively,

$$Y^* = \sqrt{\sum_{i=1}^D Y_i^2} \quad \text{and} \quad Y^* = U \cdot \operatorname{diag}(\sigma) \cdot V^T. \quad (\text{A.3})$$

**Proof.** Since (A.1) is strictly convex, its solution must be unique. That is, we only need to show that (A.2) is a solution of (A.1).

Recall that  $X_i$  minimizes (A.1) if and only if 0 is a subgradient of (A.1) at  $X_i$ , i.e.,

$$0 \in X_i - Y_i + \lambda \partial \|X^*\|_* \frac{X_i}{X^*}, i \leq D, \quad (\text{A.4})$$

with  $\partial$  being a subgradient of the nuclear norm that can be characterized by [22, 44]

$$\partial \|X^*\|_* = \{UV^T + W : X^* = U\Sigma V^T, U^T W = 0, W V = 0, \|W\|_2 \leq 1\}. \quad (\text{A.5})$$

On the other hand, let  $\Sigma_0$  (resp.  $\Sigma_l$ ) be the singular values of  $Y^*$  larger (resp. smaller) than  $\lambda$ , and  $U_0, V_0$  (resp.  $U_l, V_l$ ) be the associated singular vectors, then we have

$$Y^* = U_0 \Sigma_0 V_0^T + U_l \Sigma_l V_l^T, \quad (\text{A.6})$$

and from (A.2),

$$T_\lambda(Y_i) = [U_0(\Sigma_0 - \lambda I) V_0^T] \frac{Y_i}{Y^*}, i \leq D. \quad (\text{A.7})$$

Therefore,

$$T_\lambda(Y)^* = [U_0(\Sigma_0 - \lambda I) V_0^T]. \quad (\text{A.8})$$

From (A.7) and (A.8), we have

$$\frac{T_\lambda(Y_i)}{T_\lambda(Y)^*} = \frac{Y_i}{Y^*}, i \leq D. \quad (\text{A.9})$$

Combining (A.6), (A.7) and (A.9),

$$Y_i - T_\lambda(Y_i) = \frac{Y_i}{Y^*} \{Y^* - [U_0(\Sigma_0 - \lambda I) V_0^T]\} = \frac{T_\lambda(Y_i)}{T_\lambda(Y)^*} \lambda [U_0 V_0^T + U_l (\lambda^{-1} \Sigma_l) V_l^T]. \quad (\text{A.10})$$

That is,

$$Y_i - T_\lambda(Y_i) = \frac{T_\lambda(Y_i)}{T_\lambda(Y)^*} \lambda (U_0 V_0^T + W) \quad \text{with} \quad W = U_l (\lambda^{-1} \Sigma_l) V_l^T. \quad (\text{A.11})$$

Next, by the facts that (i)  $U_0, V_0$  are the singular vectors of  $T_\lambda(Y)^*$  from (A.8) and (ii)  $\|W\|_2 \leq 1$  since  $\|\lambda^{-1} \Sigma_l\|_2 \leq 1$ , (iii)  $U_0^T W = 0$  and  $W V_0 = 0$ , we conclude from (A.5)

$$Y_i - T_\lambda(Y_i) \in \lambda \partial \|T_\lambda(Y)^*\|_* \frac{T_\lambda(Y_i)}{T_\lambda(Y)^*}, i \leq D. \quad (\text{A.12})$$

Therefore,  $T_\lambda(Y_i)$  satisfies (A.4), and the theorem is proved.

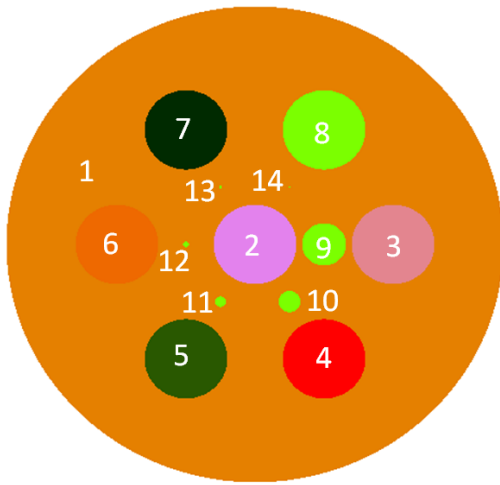
$$\begin{array}{c}
 \boxed{X} = \boxed{\text{Low-Rank } X_L} + \boxed{\text{Sparse } X_S} \\
 \begin{bmatrix} 2 & 1 & 1 \\ 1 & 2 & 1 \\ 1 & 1 & 2 \end{bmatrix} = \begin{bmatrix} 1 & 1 & 1 \\ 1 & 1 & 1 \\ 1 & 1 & 1 \end{bmatrix} + \begin{bmatrix} 1 & 0 & 0 \\ 0 & 1 & 0 \\ 0 & 0 & 1 \end{bmatrix} \\
 \boxed{R(X)=3, \#(X)=9} \quad \boxed{R(X_L)=1} \quad \boxed{\#(X_S)=3}
 \end{array}$$

**Observation**: although  $X$  is neither low-rank nor sparse,  $X$  is the superposition of low-rank  $X_L$  and sparse  $X_S$ .

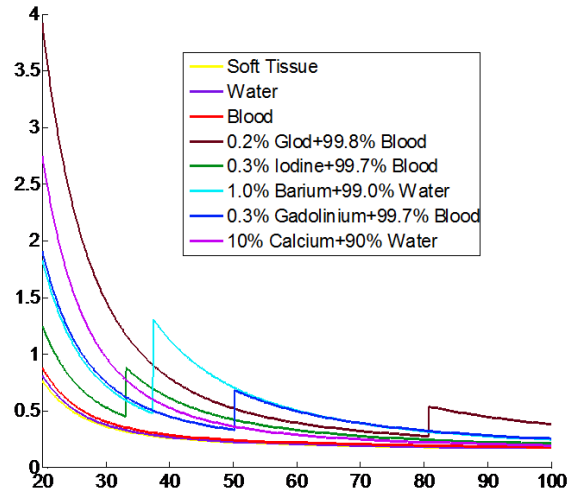
**Figure 1.** Rank-and-Sparsity Decomposition.  $R(X)$ : matrix rank;  $\#(X)$ : number of nonzeros.

**Table 1.** Parameters of the objects in the phantom (Figure 2) and the names of the associated materials.

Object	Center (cm)	Radius (cm)	Base Material
1	(0.0000, 0.0000)	1.0000	Soft Tissue
2	( 0.0000, 0.0000)	0.1667	Water
3	( 0.5556, 0.0000)	0.1667	Blood
4	( 0.2778,-0.4811)	0.1667	0.2% Gold+99.8% Blood
5	(-0.2778,-0.4811)	0.1667	0.3% Iodine+99.7% Blood
6	(-0.5556, 0.0000)	0.1667	1.0% Barium+99.0% Water
7	(-0.2778, 0.4811)	0.1667	0.3% Gadolinium+99.7% Blood
8	( 0.2778, 0.4811)	0.1667	10% Calcium+90% Water
9	(0.2778, 0.0000)	0.0899	10% Calcium+90% Water
10	( 0.1389,-0.2406)	0.0444	10% Calcium+90% Water
11	(-0.1389,-0.2406)	0.0222	10% Calcium+90% Water
12	(0.1389, 0.0000)	0.0111	10% Calcium+90% Water
13	(-0.1389, 0.2406)	0.0056	10% Calcium+90% Water
14	( 0.1389, 0.2406)	0.0028	10% Calcium+90% Water



(a)



(b)

**Figure 2.** Multi-energy CT Phantom. (a) The geometric setting of the phantom with 14 objects (Table 1), and (b) plots of the linear attenuation coefficients of the employed 8 base materials with respect to energies (The x-axis unit: KeV; the y-axis unit:  $\text{cm}^{-1}$ ).

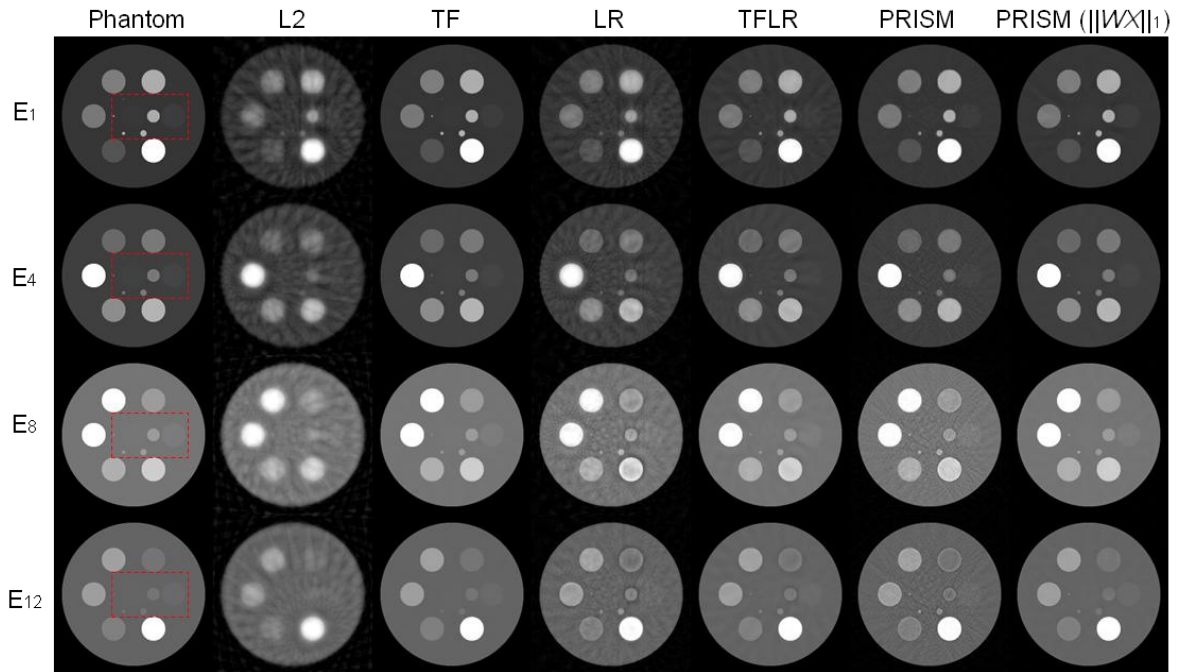


**Figure 3.** PRISM *v.s.* Other Methods. Column 1-7 correspond to the multi-energy phantom (Phantom), L2 regularization (L2), tight frame regularization (TF), rank regularization (LR), tight frame and rank regularization (TFLR), PRISM without regularizing the total image (PRISM), and PRISM with tight frame regularization of the total image (PRISM  $\|WX\|_1$ ) respectively. Row 1-4 are from the 1<sup>st</sup>, 4<sup>th</sup>, 8<sup>th</sup>, and 12<sup>th</sup> energy bin respectively. The images in each row have the same display window as the first image in that row. (See Figure 4 for the zoom-in image details inside the red squares.)

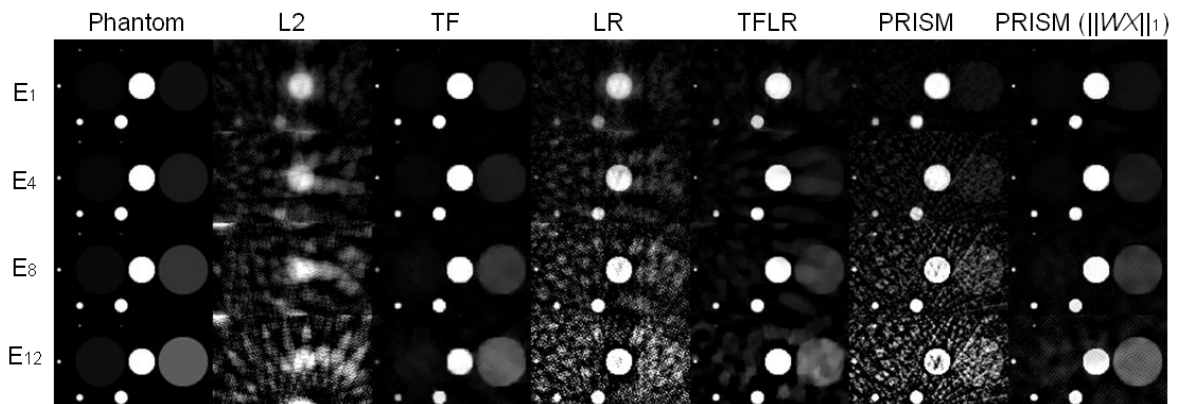


**Figure 4.** PRISM *v.s.* Other Methods. The images are the zoom-in details inside the red squares in Figure 3. Column 1-7 correspond to the multi-energy phantom (Phantom), L2 regularization (L2), tight frame regularization (TF), rank regularization (LR), tight frame and rank regularization (TFLR), PRISM without regularizing the total image (PRISM), and PRISM with tight frame regularization of the total image (PRISM  $\|WX\|_1$ ) respectively. Row 1-4 are from the 1<sup>st</sup>, 4<sup>th</sup>, 8<sup>th</sup>, and 12<sup>th</sup> energy bin respectively. The images in each row have the same display window as the first image in that row.



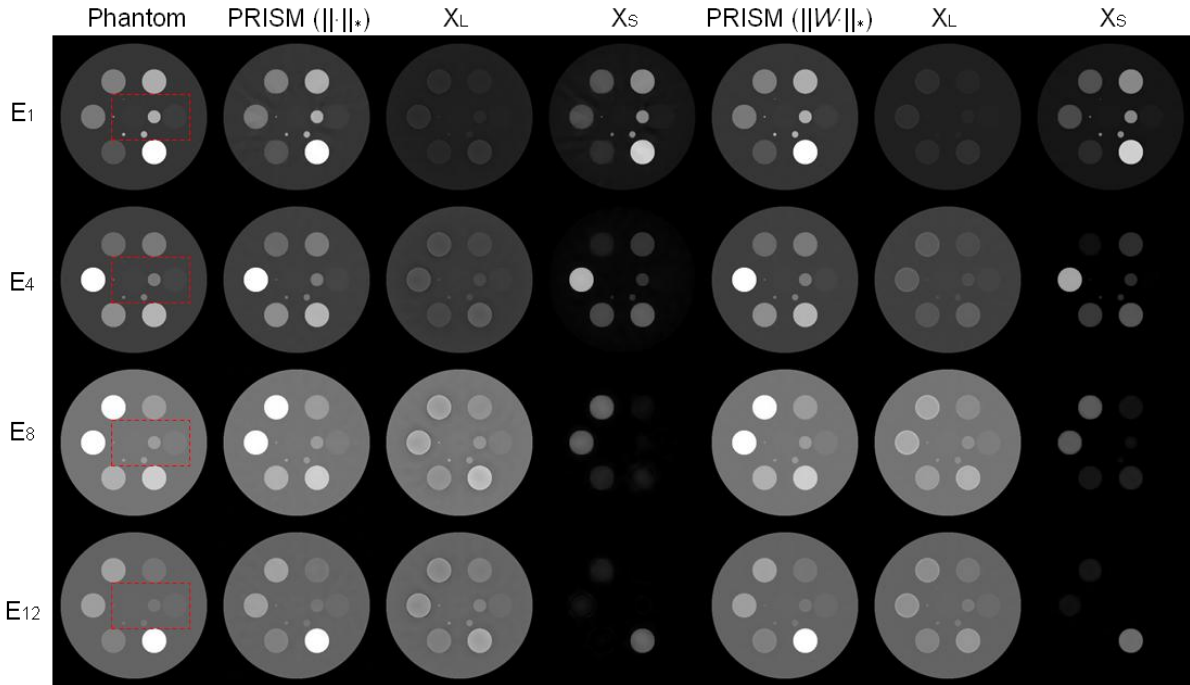


**Figure 5.** Image Rank *v.s.* Generalized Rank in PRISM. Column 1 is the multi-energy phantom (Phantom). Column 2-4 is from PRISM with image rank regularization (PRISM  $\|\cdot\|_*$ ): the total image, the low-rank background component ( $X_L$ ), the sparse variation component ( $X_S$ ). Column 5-7 is from PRISM with transformed rank regularization (PRISM  $\|W\cdot\|_*$ ): the total image, the low-rank background component ( $X_L$ ), the sparse variation component ( $X_S$ ). Row 1-4 is from the 1<sup>st</sup>, 4<sup>th</sup>, 8<sup>th</sup>, and 12<sup>th</sup> energy bin respectively. The images in each row have the same display window as the first image in that row. (See Figure 6 for the zoom-in image details inside the red squares.)

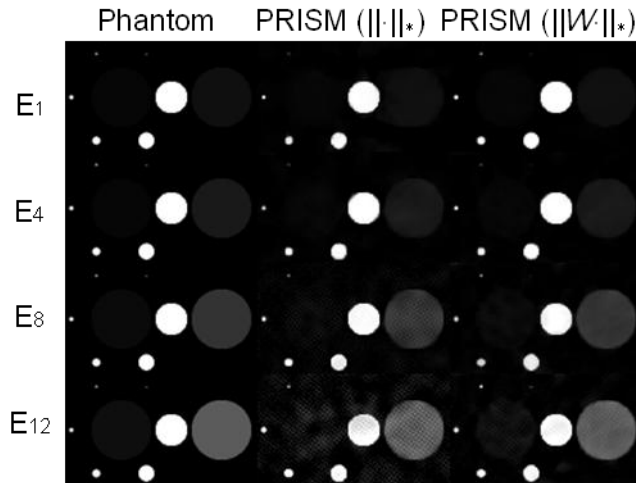


**Figure 6.** Image Rank *v.s.* Generalized Rank in PRISM. The images are the zoom-in details inside the red squares in Figure 5. Column 1 is the multi-energy phantom (Phantom). Column 2-4 is from PRISM with image rank regularization (PRISM  $\|\cdot\|_*$ ): the total image, the low-rank background component ( $X_L$ ), the sparse variation component ( $X_S$ ). Column 5-7 is from PRISM with transformed rank regularization (PRISM  $\|W\cdot\|_*$ ): the total image, the low-rank background component ( $X_L$ ), the sparse variation component ( $X_S$ ). Row 1-4 is from the 1<sup>st</sup>, 4<sup>th</sup>, 8<sup>th</sup>, and 12<sup>th</sup> energy bin respectively. The images in each row have the same display window as the first image in that row.

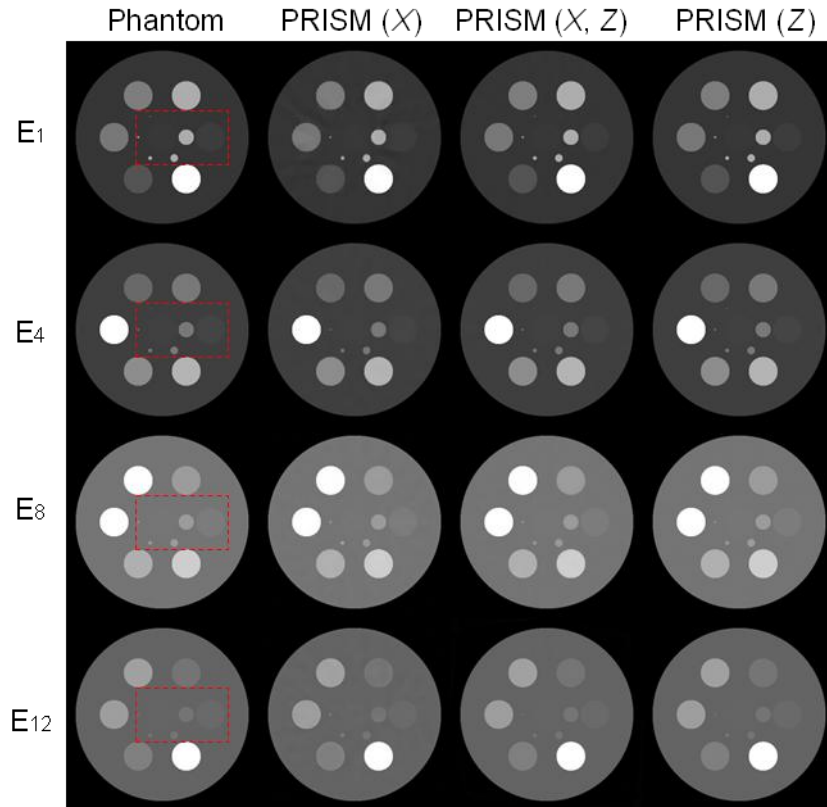


**Figure 7.** PRISM with Intensity/Spectral Priors for Multi-energy CT. Column 1-4 corresponds to the multi-energy phantom (Phantom), PRISM without spectral priors (PRISM (X)), PRISM with partial spectral priors (PRISM (X, Z)), and PRISM with full spectral priors (PRISM (Z)) respectively. Row 1-4 is from the 1<sup>st</sup>, 4<sup>th</sup>, 8<sup>th</sup>, and 12<sup>th</sup> energy bin respectively. The images in each row have the same display window as the first image in that row. (See Figure 8 for the zoom-in image details inside the red squares.)

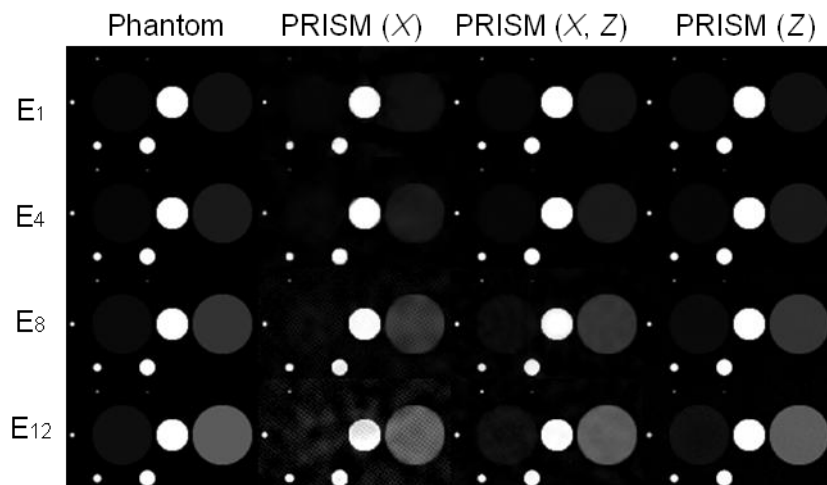


**Figure 8.** PRISM with Intensity/Spectral Priors for Multi-energy CT. The images are the zoom-in details inside the red squares in Figure 7. Column 1-4 corresponds to the multi-energy phantom (Phantom), PRISM without spectral priors (PRISM (X)), PRISM with partial spectral priors (PRISM (X, Z)), and PRISM with full spectral priors (PRISM (Z)) respectively. Row 1-4 is from the 1<sup>st</sup>, 4<sup>th</sup>, 8<sup>th</sup>, and 12<sup>th</sup> energy bin respectively. The images in each row have the same display window as the first image in that row.

## References

- [1] Boll, D.T., et al., "Spectral coronary multidetector computed tomography angiography: Dual benefit by facilitating plaque characterization and enhancing lumen depiction", *Journal Of Computer Assisted Tomography*, **30**, 804-811 (2006).
- [2] J. Jakubek, "Semiconductor Pixel detectors and their applications in life sciences", *JINST*, **4**, P03013 (2009).
- [3] D.M. Hoffman et al, Direct conversion energy discriminating CT detector with over-ranging correction, US Patent Application No. US 2008/0304618 A1 (2008).
- [4] R. Proksa, Quantitative material decomposition for spectral CT, US Patent No. 7, 627,080 B2 (2009).
- [5] J. P. Schlomka, et al., "Experimental feasibility of multi-energy photon-counting K-edge imaging in pre-clinical computed tomography", *Phys. Med. Biol.*, **53**, 4031-47 (2008).
- [6] N.G. Anderson, et al., "Spectroscopic (multi-energy) CT distinguishes iodine and barium contrast material in MICE", *Eur. Radiol.*, **20**, 2126-34 (2010).
- [7] J. F. Hainfeld, et al., "Gold nanoparticles: a new X-ray contrast agent", *Br. J. Radiol.*, **79**, 248-53 (2006).
- [8] D. B. Akolekar, G. Foran, and S. K. Bhargava, "X-ray absorption spectroscopic studies on gold nanoparticles in mesoporous and microporous materials", *J. Synchrotron Radiat.*, **11**, 284-90 (2004).
- [9] Z. Wang, L. Wu, and W. Cai, "Size-tunable synthesis of monodisperse water-soluble gold nanoparticles with high X-ray attenuation", *Chemistry*, **16**, 1459-63 (2010).
- [10] C. Xu, G.A. Tung, and S. Sun, "Size and concentration effect of gold nanoparticles on X-ray attenuation as measured on computed tomography", *Chem. Mater.*, **20**, 4167-69 (2008).
- [11] E. J. Candès, J. Romberg, and T. Tao, "Robust uncertainty principles: exact signal reconstruction from highly incomplete frequency information", *IEEE Trans. Inf. Theory*, **52**, 489-509 (2006).
- [12] D. L. Donoho, "Compressed sensing", *IEEE Trans. Inf. Theory*, **52**, 1289-306 (2006).
- [13] R. Tibshirani, "Regression shrinkage and selection via the Lasso", *Journal of the Royal Statistical Society. Series B*, **58**, 267-288 (1996).
- [14] L. Rudin, S. Osher, and E. Fatemi, "Nonlinear total variation based noise removal algorithms", *J. Phys. D*, **60**, 259-268 (1992).
- [15] R. Tibshirani, M. Saunders, S. Rosset and J. Zhu. "Sparsity and smoothness via the fused Lasso", *Journal of the Royal Statistical Society Series B*, **67**, 91-108 (2005).
- [16] H. Gao, and H. Zhao, "Multilevel bioluminescence tomography based on radiative transfer equation Part 2: total variation and l1 data fidelity", *Optics Express*, **18**, 2894-2912 (2010).
- [17] I. Daubechies, *Ten Lectures on Wavelets*, vol. 61 of CBMS-NSF Lecture Notes, SIAM (1992).
- [18] S. G. Mallat, *A Wavelet Tour of Signal Processing*, Academic Press (1998).
- [19] A. Ron and Z. Shen, "Affine systems in  $L_2(\mathbb{R}^d)$ : the analysis of the analysis operator", *J. Funct. Anal.*, **148**, 408-447 (1997).
- [20] I. Daubechies, B. Han, A. Ron, and Z. Shen, "Framelets: MRA-based constructions of wavelet frames", *Applied and Computational Harmonic Analysis*, **14**, 1-46 (2003).
- [21] V. Chandrasekaran, S. Sanghavi, P. Parrilo, and A. Willsky, "Rank-sparsity incoherence for matrix decomposition", arXiv:0906.2220v1 (2009).
- [22] E. J. Candès, X. Li, Y. Ma, and J. Wright, "Robust principal component analysis?", *Technical report*, Stanford University (2009).
- [23] H. Gao, J. F. Cai, Z. Shen and H. Zhao, "Robust principle component analysis based four-dimensional computed tomography". *Phys. Med. Biol.*, **56**, 3181-3198 (2011).

- [24] H. Ji, C. Liu, Z. Shen, and Y. Xu, "Robust video denoising using low rank matrix completion", *IEEE Conference on Computer Vision and Pattern Recognition (CVPR)*, San Francisco (2010).
- [25] H. Ji, Z. Shen, and Y. Xu, "Robust video restoration by joint sparse and low rank matrix approximation", Preprint (2010).
- [26] Y. Peng, et al., "RASL: robust alignment by sparse and low-rank decomposition for linearly correlated images", *IEEE Conference on Computer Vision and Pattern Recognition (CVPR)*, San Francisco (2010).
- [27] G. Liu, Z. Lin, and Y. Yu, "Robust subspace segmentation by low-rank representation", *Proceedings of the 26th International Conference on Machine Learning (ICML)*, Haifa, Israel (2010).
- [28] K. Min, Z. Zhang, J. Wright, and Y. Ma, "Decomposing background topics from keywords by principal component pursuit", *Proceedings of ACM International Conference on Information and Knowledge Management (CIKM)*, Toronto, Canada (2010).
- [29] G. Zhu, S. Yan, and Y. Ma, "Image tag refinement towards low-rank, content-tag prior and error sparsity", *Proceedings of ACM Multimedia*, Firenze, Italy (2010).
- [30] Z. Zhang, X. Liang, A. Ganesh, and Y. Ma, "TILT: transform invariant low-rank textures", *Proceedings of Asian Conference on Computer Vision*, Queenstown, New Zealand (2010).
- [31] L. Wu et al., "Robust photometric stereo via low-rank matrix completion and recovery", *Proceedings of Asian Conference on Computer Vision*, Queenstown, New Zealand (2010).
- [32] T. Buzug, *Computed Tomography: From Photon Statistics to Modern Cone-Beam CT*, Springer-Verlag (2008).
- [33] B. Recht, M. Fazel, and P. Parrilo, "Guaranteed Minimum-Rank Solutions of Linear Matrix Equations via Nuclear Norm Minimization", *SIAM Review*, **52**, 471-501 (2010).
- [34] E. J. Candès, and B. Recht, "Exact matrix completion via convex optimization," *Foundations of Computational Mathematics*, **9**, 717-772 (2009).
- [35] B. Dong and Z. Shen, "MRA-based wavelet frames and applications", *UCLA CAM Report*, 10-69 (2010).
- [36] S. Osher, M. Burger, D. Goldfarb, J. Xu, and W. Yin, "An iterative regularization method for total variation-based image restoration", *Multiscale Model. Simul.*, **4**, 460-489 (2005).
- [37] T. Goldstein and S. Osher, "The split Bregman algorithm for  $l_1$  regularized problems", *SIAM J. Imaging Sci.*, **2**, 323-343 (2009).
- [38] J. F. Cai, S. Osher, and Z. Shen, "Split Bregman methods and frame based image restoration", *Multiscale Model. Simul.*, **8**, 337-369 (2009).
- [39] H. Gao, H. Zhao and S. Osher, "Quantitative photoacoustic tomography", *UCLA CAM Report*, 11-28 (2011).
- [40] G. Wang, Y. Ye, and H. Yu, *Interior tomography and instant tomography reconstruction from truncated limited angle projection data*. US Patent 7,697,658 B2 (2010).
- [41] Y. B. Ye, H. Y. Yu, Y. C. Wei, and G. Wang, "A general local reconstruction approach based on a truncated Hilbert transform", *Int. J. Biomed. Imaging*, Article ID 63634 (2007).
- [42] H. Kudo, M. Courdurier, F. Noo, and M. Defrise, "Tiny *a priori* knowledge solves the interior problem in computed tomography", *Phys. Med. Biol.*, **53**, 2207-2231 (2008).
- [43] H. Yu and G. Wang, "Compressed sensing based Interior tomography", *Phys. Med. Biol.*, **54**, 2791-805 (2009).
- [44] J. F. Cai, E.J. Candès, and Z. Shen, "A singular value thresholding algorithm for matrix completion", *SIAM J. Optimiz.*, **20**, 1956-1982 (2010).